Computational Mechanics (2022) 70:965–976
https://doi.org/10.1007/s00466-022-02193-8

ORIGINAL PAPER

A large deformation isogeometric continuum shell formulation incorporating finite strain elastoplasticity

Ning Liu[1] · Ming-Chen Hsu[2] · Jim Lua[1] · Nam Phan[3]

Received: 18 March 2022 / Accepted: 3 May 2022 / Published online: 11 June 2022

Abstract
An isogeometric large-deformation continuum shell formulation incorporating finite strain elastoplasticity is presented in this work. The proposed method is based on the multiplicative decomposition of the deformation gradient into the elastic and plastic contributions in a total Lagrangian framework. The standard return mapping algorithm with the backward Euler time integration technique is adopted to solve the 3D elastoplastic constitutive equations. The classical J_2 von Mises plasticity model with isotropic hardening is implemented to describe the nonlinear material behavior. The results of several benchmark studies are illustrated to showcase the computational accuracy and solution robustness of the proposed formulation.

Keywords Isogeometric analysis · Finite strain multiplicative plasticity · Continuum shell · Large deformation · Elastoplastic analysis

1 Introduction

Many real-world engineering structures can be categorized as thin-walled applications, and engineers often rely on computationally efficient shell elements to perform an initial analysis and determine the load-carrying capacity of the structure. While the linear elastic shell analysis is adopted in many cases, it is often insufficient due to the large-deformation nature of the problem or the nonlinear material behavior as a result of locally concentrated loading. In the latter, a high-fidelity elastoplastic constitutive model is needed to accurately capture the material degradation. An example of such a scenario encountered in engineering is low-cycle fatigue analysis, which deals with stresses beyond yielding and sophisticated material behaviors such as hardening. In such cases, a plasticity coupled shell analysis is required.

The incorporation of finite-to-large strain elastoplastic constitutive models into shell formulations is very challenging, and a variety of research efforts has been devoted to the advancement in this subject. In the modeling of the elastoplastic material response using thin shells (e.g., of the Kirchhoff–Love (KL) shell type), two approaches are typically adopted, one being the deployment of integration points in the through-thickness direction of the shell body and the use of 3D stress-based elastoplastic material models [1–8], and the other being the employment of stress resultant based plasticity models in which the constitutive material relations are directly formulated towards obtaining the stress resultants [9–14]. While the latter extends the 2D geometric description into constitutive models and seems to be a more straightforward path to take, the derivation of the inelastic constitutive models directly for stress resultants is rather complicated, even for the simplest case of J_2 plasticity. The level of complexity arises when hardening is involved, leading to the so-called Ilyushin–Shapiro constitutive relations [13]. Due to the difficulties in the mathematical derivation and numerical implementation, researchers are widely in favor of the stress-based approach, where 3D plasticity models for solids with standard return mapping algorithms are directly applicable.

Although thin shell elements [15] are computationally efficient, they sometimes do not suffice in the complex structural design and analysis workflow, mainly due to the need to acquire 3D high-fidelity strains and stresses in order to comprehensively evaluate the structural integrity and multiaxial

✉ Ning Liu
nliu@gem-innovation.com

[1] Global Engineering and Materials, Inc., Princeton, NJ 08540, USA

[2] Department of Mechanical Engineering, Iowa State University, Ames, IA 50011, USA

[3] Structures Division, Naval Air Systems Command (NAVAIR), Patuxent River, MD 20670, USA

fatigue life [16,17]. This, in turn, gives rise to the development of shell formulations of the continuum type [18–23] and the blended type [24–28], which features accurate predictions of the full 3D strain and stress tensors, including the components in the transverse directions and through the thickness of the shell body. Worth mentioning is a recently developed blended shell formulation [24–26] that couples KL shells and continuum shells in a non-matching and nonlinear analysis setting so that it can compute accurate 3D strains and stresses without compromising computational efficiency. The primary advantage of using continuum shells over solids to obtain high-fidelity 3D strains and stresses of thin-walled structures arises from the efficiency in the geometric modeling process. The continuum shells are formulated based on a reference surface, and therefore only the surface modeling of a thin-walled structure is needed. This greatly simplifies the modeling procedure compared to using solid elements, where a full 3D description of the geometry is required. An added benefit of the continuum shell approach is that it significantly eases the coupling mechanism between KL shells and the solid-like counterpart, since both are formulated under curvilinear coordinates with analogous definitions of surface tangential and normal vectors. More details of the coupling formulation can be found in Liu et al. [24].

As is commonly an issue in the analysis group, the process of geometry repair and the generation of an approximate finite element mesh from computer-aided design (CAD) consume the majority of the analysis time. This primarily results from the use of different technologies between the design and analysis parties and constitutes a major bottleneck to the interoperability between CAD and finite element analysis (FEA) technologies. Driven by the need in design and analysis alike, the advent of isogeometric analysis (IGA) [29] bridges the gap in the sense that it uses the same high-order spline basis functions to represent the original geometry and the physics-based solution fields in analysis. Moreover, the high-order continuities of splines offer other significant benefits beyond the perspective of exact geometric representations, such as the straightforward implementation of high-order differential operators [30–34], as is the case of Kirchhoff–Love thin shell formulations where C^1 global smoothness is required [35–42]. Additionally, it has been shown that the use of spline-based IGA provides significantly improved per-degree-of-freedom solution accuracy over standard FEA [27,31,43–52], and the IGA approach has since been used to solve the most challenging science and engineering problems [53–83]. Nevertheless, the development with regards to IGA-based plastic shell formulations has been rare. This includes a recently proposed isogeometric stress-based elastoplastic KL shell formulation with the plane stress assumption imposed in an iterative fashion [1,2] and later applied to multi-patch analysis [84]. In addition, an isogeometric solid shell element formulated in an updated Lagrangian framework has been presented with emphasis on locking alleviation by resorting to the assumed natural strain technique [85], where the applied plasticity model pertains to the small strain regime.

The primary aim of this work is to extend the isogeometric large-deformation continuum shell formulation presented in Liu et al. [18] to the finite strain plasticity regime. The multiplicative decomposition of the deformation gradient into the elastic and plastic parts, along with the classical J_2 von Mises plasticity with isotropic hardening [86], is adopted in a total Lagrangian framework. The standard backward Euler time integration scheme with return mapping is employed to solve the 3D elastoplastic constitutive equations.

This paper is organized as follows. In Sect. 2, we briefly review the isogeometric large-deformation continuum shell formulation. In Sect. 3, the finite strain plasticity model, along with details on the numerical implementation aspects, is given. A discussion on the adopted J_2 plasticity model with isotropic hardening is also included. The proposed formulation is then applied in Sect. 4 to a variety of benchmark tests to demonstrate its accuracy and robustness. Finally, Sect. 5 concludes the paper with some remarks.

2 Isogeometric continuum shell formulation

We start the derivation by briefly introducing the isogeometric large-deformation continuum shell formulation [18,24]. In the following, we use italic letters (e.g., a, A) to represent scalars, lowercase bold letters (e.g., $\mathbf{a}$) to represent vectors, and uppercase bold letters (e.g., $\mathbf{A}$) to represent second-order tensors. We refer the geometric variables denoted by $\mathring{(\cdot)}$ to the reference (i.e., undeformed) configuration. Compact notations are used only when convenient for the presentation of general equations, while the detailed derivations are written in index notation. The Latin indices such as i, j, k, and l take on values of $\{1, 2, 3\}$, and the Greek indices such as α and β take on values of $\{1, 2\}$; summation convention of repeated indices is employed unless otherwise stated.

We describe a material point within the shell body in the reference configuration Ω_0 by its position vector $\mathring{\mathbf{x}}(\xi_1, \xi_2, \xi_3)$, with ξ_1 and ξ_2 the convective curvilinear coordinates in the in-plane directions, and ξ_3 the through-thickness coordinate of the parameter space P (cf. Fig. 1). Taking the bottom surface of the continuum shell as the reference surface, the undeformed position vector can be further described using the projected point at the bottom surface, $\mathring{\mathbf{r}}$, and the unit thickness director normal to the shell bottom surface, $\mathring{\mathbf{a}}_3$,

$$\mathring{\mathbf{x}}(\xi_1, \xi_2, \xi_3) = \mathring{\mathbf{r}}(\xi_1, \xi_2) + \xi_3 \mathring{\mathbf{a}}_3(\xi_1, \xi_2), \tag{1}$$

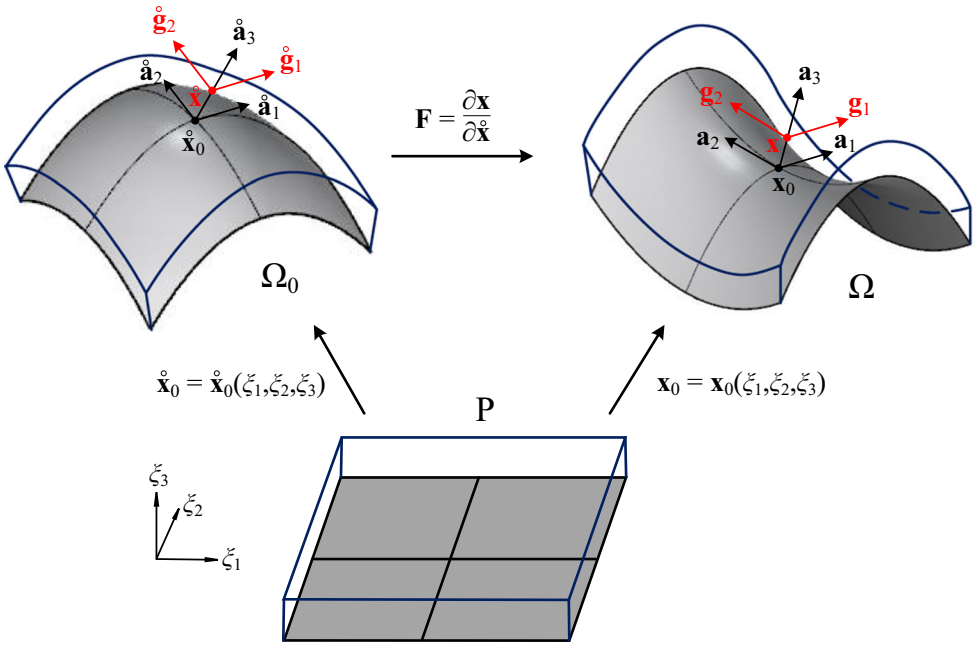

Fig. 1 A schematic view of the mapping between the parametric, reference (i.e., undeformed) and current (i.e., deformed) configurations

where $\xi_3 \in [0, t]$ and t denotes the total thickness of the shell. We denote $\mathring{\mathbf{a}}_\alpha = \mathring{\mathbf{r}}_{,\alpha}$ as the in-plane base vectors of the bottom surface in the reference configuration, where $(\cdot)_{,\alpha} = \partial(\cdot)/\partial\xi_\alpha$. The unit normal vector $\mathring{\mathbf{a}}_3$ can then be derived as

$$\mathring{\mathbf{a}}_3 = \frac{\mathring{\mathbf{a}}_1 \times \mathring{\mathbf{a}}_2}{\|\mathring{\mathbf{a}}_1 \times \mathring{\mathbf{a}}_2\|}. \tag{2}$$

In order to describe the motion of an arbitrary material point in the continuum shell body, it is convenient to define a set of covariant base vectors. Specifically, the base vectors at any point in the original shell configuration can be expressed as $\mathring{\mathbf{g}}_i = \mathring{\mathbf{x}}_{,i}$, with $(\cdot)_{,i} = \partial(\cdot)/\partial\xi_i$, and further expanded as

$$\mathring{\mathbf{g}}_\alpha = \mathring{\mathbf{a}}_\alpha + \xi_3 \mathring{\mathbf{a}}_{3,\alpha}\,, \tag{3}$$

$$\mathring{\mathbf{g}}_3 = \mathring{\mathbf{a}}_3. \tag{4}$$

Having defined the covariant base vectors, their dual base vectors (i.e., the contravariant base vectors) can be computed according to the Kronecker delta relation, $\mathring{\mathbf{g}}_i \cdot \mathring{\mathbf{g}}^j = \delta_i^j$. The position vector $\mathbf{x}(\xi_1, \xi_2, \xi_3)$ in the current configuration Ω can be related to the reference position vector $\mathring{\mathbf{x}}$ through the displacement vector $\mathbf{u}$, i.e., $\mathbf{x} = \mathring{\mathbf{x}} + \mathbf{u}$. The deformed covariant base vectors can then be written as

$$\mathbf{g}_i = \mathbf{x}_{,i} = \mathring{\mathbf{g}}_i + \mathbf{u}_{,i}. \tag{5}$$

Finally, we arrive at the deformation gradient between the reference and current configurations in a total Lagrangian framework, $\mathbf{F} = \mathbf{g}_i \otimes \mathring{\mathbf{g}}^i$, from which the Green–Lagrange strain tensor can be easily computed as

$$\mathbf{E} = \frac{1}{2}\left(\mathbf{F}^{\mathrm{T}}\mathbf{F} - \mathbf{I}\right), \tag{6}$$

with $\mathbf{I}$ the second-order identity tensor. Let $g_{ij} = \mathbf{g}_i \cdot \mathbf{g}_j$ be the metric coefficients of the first fundamental form. The Green–Lagrange strain tensor then becomes

$$\mathbf{E} = \frac{1}{2}\left(g_{ij} - \mathring{g}_{ij}\right)\mathring{\mathbf{g}}^i \otimes \mathring{\mathbf{g}}^j = E_{ij}\mathring{\mathbf{g}}^i \otimes \mathring{\mathbf{g}}^j. \tag{7}$$

where the specific strain component E_{ij} can be computed based on the reference local covariant vectors and the current displacement derivatives as

$$E_{ij} = \frac{1}{2}\left(\mathring{\mathbf{g}}_i \cdot \mathbf{u}_{,j} + \mathring{\mathbf{g}}_j \cdot \mathbf{u}_{,i} + \mathbf{u}_{,i} \cdot \mathbf{u}_{,j}\right). \tag{8}$$

Equation (7) essentially describes the variation of surface metric tensors due to structural deformation.

With the Green–Lagrange strain tensor at hand, the energetically conjugate second Piola–Kirchhoff stress tensor $\mathbf{S}$ can be obtained based on the adopted hyperelastic-based plasticity model, as elaborated in the next section. Note that, since material models are typically formulated with respect to the Cartesian coordinate system, the above strain tensor needs to be transformed from the curvilinear system to the element local system

$$E^e_{ij} = E_{kl}\left(\mathring{\mathbf{g}}^k \cdot \mathbf{e}_i\right)\left(\mathring{\mathbf{g}}^l \cdot \mathbf{e}_j\right), \tag{9}$$

where E^e_{ij} are the coefficients of the Green–Lagrange strain tensor with respect to the local Cartesian base vectors defined as

$$\mathbf{e}_1 = \frac{\mathring{\mathbf{g}}_1}{\|\mathring{\mathbf{g}}_1\|}\,, \quad \mathbf{e}_2 = \frac{\mathring{\mathbf{g}}_2 - \left(\mathring{\mathbf{g}}_2 \cdot \mathbf{e}_1\right)\mathbf{e}_1}{\|\mathring{\mathbf{g}}_2 - \left(\mathring{\mathbf{g}}_2 \cdot \mathbf{e}_1\right)\mathbf{e}_1\|}\,, \quad \mathbf{e}_3 = \mathbf{e}_1 \times \mathbf{e}_2. \tag{10}$$

Transformations of the stress tensor $\mathbf{S}$ and the deformation gradient $\mathbf{F}$ follow in an analogous fashion.

It is now straightforward to arrive at the variational formulation of the isogeometric continuum shell based on the principle of virtual work, in which the contribution of the body force is neglected for brevity:

$$\delta W = \delta W^{\text{int}} - \delta W^{\text{ext}} = \int_{\Omega_0} \delta\mathbf{E} : \mathbf{S}\, \mathrm{d}\Omega_0 - \int_{\Gamma_0^{\text{h}}} \delta\mathbf{u} \cdot \mathbf{h}\, \mathrm{d}\Gamma_0^{\text{h}} = 0\,, \tag{11}$$

where W, W^{int} and W^{ext} represent the total, internal and external work, respectively, δ denotes the variation with respect to the virtual displacement variable $\delta\mathbf{u}$, Ω_0 is the shell volume in the reference configuration, $\mathrm{d}\Omega_0 = \sqrt{\det\left(\mathring{g}_{ij}\right)}\mathrm{d}\xi_1\mathrm{d}\xi_2\mathrm{d}\xi_3$, $\mathbf{h}$ is the surface traction, and Γ_0^{h} is the reference boundary to which $\mathbf{h}$ is applied.

An incremental iterative solution scheme (e.g., cylindrical arc-length control [87]) can be adopted to solve the above nonlinear system, in which the derivation of the tangential stiffness necessitates the linearization of the internal work

$$\mathcal{D}\delta W^{\text{int}} = \int_{\Omega_0} \left(\delta\mathbf{E} : \mathbb{C}\mathcal{D}\mathbf{E} + \mathcal{D}\delta\mathbf{E} : \mathbf{S}\right)\, \mathrm{d}\Omega_0. \tag{12}$$

Additional details of the formulation and numerical implementation aspects can be found in Liu et al. [18,24].

3 Finite strain hyperelastic-based plasticity

The adopted finite strain hyperelastic plasticity model is based on the framework of multiplicative decomposition of the deformation gradient into the elastic and plastic contributions and the concept of intermediate stress-free configurations [88,89]. To describe the plastic flow and nonlinear material response, the classical 3D J_2 von Mises rate-independent plasticity model along with isotropic hardening is employed.

According to the notion of an intermediate stress-free configuration, the deformation gradient $\mathbf{F}$ is decomposed as

$$\mathbf{F} = \mathbf{F}^{\text{e}}\mathbf{F}^{\text{p}}\,, \tag{13}$$

where $\mathbf{F}^{\text{e}}$ and $\mathbf{F}^{\text{p}}$ denote the elastic and plastic contributions of the deformation gradient, respectively. This decomposition can be regarded as a purely plastic deformation to an intermediate stress-free configuration, based on which the elastic response can be characterized.

Following the decomposition described in Eq. (13), the elastic left and plastic right Cauchy–Green (CG) deformation tensors are introduced respectively as

$$\mathbf{b}^{\text{e}} = \mathbf{F}^{\text{e}}\left(\mathbf{F}^{\text{e}}\right)^{\text{T}}\,, \quad \mathbf{C}^{\text{p}} = \left(\mathbf{F}^{\text{p}}\right)^{\text{T}}\mathbf{F}^{\text{p}}\,. \tag{14}$$

A crucial relationship can be found by rearranging Eqs. (13) and (14), which yields an alternative expression of the elastic left CG deformation tensor $\mathbf{b}^{\text{e}}$ as a function of the plastic right CG deformation tensor $\mathbf{C}^{\text{p}}$,

$$\mathbf{b}^{\text{e}} = \mathbf{F}\left(\mathbf{C}^{\text{p}}\right)^{-1}\mathbf{F}^{\text{T}}\,. \tag{15}$$

Equation (15) dictates that the elastic deformation can be related to the plastic deformation through the deformation gradient. The rate of the elastic left CG deformation tensor, denoted as $\dot{\mathbf{C}}^{\text{p}}$, is then written in Lie derivative form as

$$\mathcal{L}_v\mathbf{b}^{\text{e}} = \mathbf{F}\left(\dot{\mathbf{C}}^{\text{p}}\right)^{-1}\mathbf{F}^{\text{T}}\,. \tag{16}$$

We describe the total free energy in the form of the summation of the elastic and plastic strain energies in the following form

$$\begin{aligned}\Phi\left(\mathbf{b}^{\text{e}}, J^{\text{e}}, \alpha\right) &= \Phi^{\text{e}}\left(\mathbf{b}^{\text{e}}, J^{\text{e}}\right) + \Phi^{\text{p}}\left(\alpha\right) \\ &= \int_{\Omega_0}\left(\Psi^{\text{e}}\left(\mathbf{b}^{\text{e}}, J^{\text{e}}\right) + \Psi^{\text{p}}\left(\alpha\right)\right)\, \mathrm{d}\Omega_0\,,\end{aligned} \tag{17}$$

where the elastic strain energy density Ψ^{e} is defined in terms of the elastic left deformation tensor $\mathbf{b}^{\text{e}}$ and the determinant of the elastic deformation gradient J^{e}, $J^{\text{e}} = \det[\mathbf{F}^{\text{e}}]$, and the plastic strain energy density Ψ^{p} is expressed as a function of the internal hardening variable α in the case of isotropic hardening.

For the elastic description of the adopted elastoplastic model, we employ a material model of the isotropic hyperelastic type to describe the material behavior, of which the elastic strain energy density Ψ^{e} can be further split into the volumetric (i.e., shape preserving) and deviatoric (i.e., volume preserving) contributions as

$$\Psi^{\text{e}} = \Psi^{\text{e}}_{\text{vol}} + \Psi^{\text{e}}_{\text{dev}}\,, \tag{18}$$

where

$$\Psi^{\text{e}}_{\text{vol}} = \frac{\kappa}{2}\left(\frac{(J^{\text{e}})^2 - 1}{2} - \ln J^{\text{e}}\right)\,, \tag{19}$$

$$\Psi^{\mathrm{e}}_{\mathrm{dev}} = \frac{\mu}{2}\left(\mathrm{tr}\left[\hat{\mathbf{b}}^{\mathrm{e}}\right] - 3\right) , \tag{20}$$

with tr[·] denoting the trace of a matrix, $\hat{\mathbf{b}}^{\mathrm{e}} = (J^e)^{-2/3}\mathbf{b}^{\mathrm{e}}$, κ and μ being the bulk and shear moduli of the material, respectively. From the derived elastic strain energy density function Ψ^{e}, the Cauchy stress $\boldsymbol{\sigma}$ can be directly computed [90] as

$$\begin{aligned}\boldsymbol{\sigma} &= 2J^{-1}\left(\frac{\partial \Psi^{\mathrm{e}}_{\mathrm{vol}}}{\partial \boldsymbol{b}^{\mathrm{e}}} + \frac{\partial \Psi^{\mathrm{e}}_{\mathrm{dev}}}{\partial \boldsymbol{b}^{\mathrm{e}}}\right)\boldsymbol{b}^{\mathrm{e}} \\ &= J^{-1}\left(\frac{\kappa}{2}\left(J^2-1\right)\mathbf{I} + \mu\,\mathrm{dev}\left[\hat{\mathbf{b}}^{\mathrm{e}}\right]\right) \\ &= J^{-1}\left(\boldsymbol{\tau}_{\mathrm{vol}} + \boldsymbol{\tau}_{\mathrm{dev}}\right) ,\end{aligned} \tag{21}$$

where $\mathrm{dev}\,[\cdot] = [\cdot] - \frac{1}{3}\mathrm{tr}\,[\cdot]\,\mathbf{I}$, $\boldsymbol{\tau}_{\mathrm{vol}}$ and $\boldsymbol{\tau}_{\mathrm{dev}}$ are the volumetric and deviatoric parts of the Kirchhoff stress tensor $\boldsymbol{\tau}$, respectively. We emphasize that plastic flow is isochoric in von Mises plsticity, and thus $J = J^{\mathrm{e}}$. Accordingly, the superscript 'e' is neglected for brevity. Subsequently, the second Piola–Kirchhoff stress used in the isogeometric continuum shell formulation can be computed according to the pull-back operation

$$\mathbf{S} = J\mathbf{F}^{-1}\boldsymbol{\sigma}\mathbf{F}^{-\mathrm{T}} . \tag{22}$$

In terms of the plastic deformation, we employ the classical Mises–Huber yield criterion, which is defined as a function of the deviatoric Kirchhoff stress $\boldsymbol{\tau}_{\mathrm{dev}}$,

$$f\left(\boldsymbol{\tau}_{\mathrm{dev}}, \alpha\right) = \|\boldsymbol{\tau}_{\mathrm{dev}}\| - \sqrt{\frac{2}{3}}k\left(\alpha\right) , \tag{23}$$

where $k\left(\alpha\right)$ is the hardening function.

The associative flow rule emerging from the theory of maximum plastic dissipation can be expressed as

$$\left(\dot{\mathbf{C}}^{\mathrm{p}}\right)^{-1} = -\frac{2}{3}\gamma\,\mathrm{tr}\left[\mathbf{b}^{\mathrm{e}}\right]\mathbf{F}^{-1}\mathbf{n}\mathbf{F}^{-\mathrm{T}} , \tag{24}$$

where γ is the plastic multiplier and $\mathbf{n} = \boldsymbol{\tau}_{\mathrm{dev}}/\|\boldsymbol{\tau}_{\mathrm{dev}}\|$. Moreover, the evolution of the yield stress is characterized by the rate of the hardening variable, which is defined as

$$\dot{\alpha} = \sqrt{\frac{2}{3}}\gamma . \tag{25}$$

The Karush–Kuhn–Tucker (KKT) conditions are employed to govern the loading/unloading conditions

$$\gamma \geq 0 , \quad f\left(\boldsymbol{\tau}_{\mathrm{dev}}, \alpha\right) \leq 0 , \quad \gamma f\left(\boldsymbol{\tau}_{\mathrm{dev}}, \alpha\right) = 0 . \tag{26}$$

In order to solve the above elastoplastic constitutive equations, we utilize a backward Euler time integration technique along with a standard return mapping algorithm. The detailed implementation is summarized in Tables 1 and 2.

4 Numerical examples

In this section, we select a number of challenging benchmark examples in the realm of finite-to-large strain plasticity to demonstrate the accuracy and robustness of the present isogeometric elastoplastic continuum shell formulation. Bicubic NURBS are utilized to represent the in-plane geometries, and quadratic B-splines with a single element discretization are used to describe the through-thickness kinematics of the continuum shell. A total of $p + 1$ Gaussian points are used in each direction for the integration of the governing equations, with p the polynomial order of the employed spline basis. A displacement-controlled algorithm is employed to iteratively solve the first two problems, while a cylindrical arc-length control algorithm [87] is adopted for the solution of the third problem. All the numerical examples were simulated on a hierarchical set of meshes, whereas only the meshes for the converged solutions were demonstrated.

4.1 Rectangular plate under uniaxial tension

The first benchmark example investigated here is concerned with the classical rectangular plate model subjected to uniaxial tension [1,2,91], which is used to test the formulation under plane stress necking. As illustrated in Fig. 2, the total length and width of the plate are $L = 50$ mm and $W = 10$ mm, respectively, and the thickness is $t = 1$ mm. The plate is fixed at one end and subjected to uniaxial tension at the other end. The material model employed is: Young's modulus of $E = 1.89 \times 10^5$ MPa, Poisson's ratio of $\nu = 0.29$, and a nonlinear isotropic hardening model of $k(\alpha) = 343 + (680 - 343)(1 - e^{-16.93\alpha}) + 300\alpha$. Due to symmetry, only a quarter of the plate is modeled. A mesh of 250 elements (i.e., 25 in the length direction and 10 in the width direction) is used to obtain the final solution.

The norm of the displacement vector divided by the total number of control points, $U_{\mathrm{norm}} = \sqrt{\frac{U^{\mathrm{T}}U}{n_{\mathrm{cp}}}}$, is recorded to quantitatively assess the accuracy of the present formulation. The obtained load-displacement curve is compared with the reference data [1,2] and plotted in Fig. 3, where a very good agreement is reached. Figure 4 displays the evolution of the hardening variable α on the deformed plate at several stages of the loading process. It can be seen that, once the material enters the yielding zone and before the ultimate strength is reached, plasticity initiates at the corners and the plate deforms uniformly as the plastic strain accumulates. At a certain stage after the ultimate strength is reached, the plastic strain starts to concentrate at the plate center where

Table 1 The solution scheme of the J_2 plasticity constitutive equations based on return mapping and backward Euler time integration

(1) Elastic predictor stage: given $\left(\mathbf{C}_{\mathrm{n}}^{\mathrm{p}}\right)^{-1}$, α_{n} and $\mathbf{F}_{\mathrm{n+1}}$

$\tilde{\mathbf{F}}_{\mathrm{n+1}} = J_{\mathrm{n+1}}^{-1/3}\mathbf{F}_{\mathrm{n+1}} \quad J_{\mathrm{n+1}} = \det\left[\mathbf{F}_{\mathrm{n+1}}\right]$

$\tilde{\mathbf{b}}_{\mathrm{n+1}}^{\mathrm{e,trial}} = \tilde{\mathbf{F}}_{\mathrm{n+1}}\left(\mathbf{C}_{\mathrm{n}}^{\mathrm{p}}\right)^{-1}\tilde{\mathbf{F}}_{\mathrm{n+1}}^{\mathrm{T}}$

$\boldsymbol{\tau}_{\mathrm{dev,n+1}}^{\mathrm{trial}} = \mu\mathrm{dev}\left[\tilde{\mathbf{b}}_{\mathrm{n+1}}^{\mathrm{e,trial}}\right] \quad \boldsymbol{\tau}_{\mathrm{vol,n+1}}^{\mathrm{trial}} = \frac{\kappa}{2}\left(J_{\mathrm{n+1}}^{2}-1\right)\mathbf{I}$

(2) Check yielding conditions:

if $f_{\mathrm{n+1}}^{\mathrm{tr}} = \|\boldsymbol{\tau}_{\mathrm{dev,n+1}}^{trial}\| - \sqrt{\frac{2}{3}}k\left(\alpha_{\mathrm{n}}\right) \le 0$ then

set $(\cdot)_{\mathrm{n+1}} = (\cdot)_{\mathrm{n+1}}^{\mathrm{trial}}$ and exit

else go to the plastic corrector stage (3)

(3) Plastic corrector:

Solve for $\triangle\gamma \ge 0$ from the equation below

$$f_{\mathrm{n+1}}^{\mathrm{trial}} = \|\boldsymbol{\tau}_{\mathrm{dev,n+1}}^{trial}\| - \sqrt{\frac{2}{3}}k\left(\alpha_{\mathrm{n}} + \sqrt{\frac{2}{3}}\triangle\gamma\right) - \frac{2}{3}\triangle\gamma\mu\mathrm{tr}\left[\tilde{\mathbf{b}}_{\mathrm{n+1}}^{\mathrm{e,trial}}\right] = 0$$

Update state variables

$\boldsymbol{\tau}_{\mathrm{vol,n+1}} = \boldsymbol{\tau}_{\mathrm{vol,n+1}}^{\mathrm{trial}}$

$\boldsymbol{\tau}_{\mathrm{dev,n+1}} = \boldsymbol{\tau}_{\mathrm{dev,n+1}}^{\mathrm{trial}} - \frac{2}{3}\triangle\gamma\mu\mathrm{tr}\left[\tilde{\mathbf{b}}_{\mathrm{n+1}}^{\mathrm{e,trial}}\right]\mathbf{n}_{\mathrm{n+1}}^{\mathrm{trial}}$

$\boldsymbol{\sigma}_{\mathrm{n+1}} = \frac{1}{J}\left(\boldsymbol{\tau}_{\mathrm{vol,n+1}} + \boldsymbol{\tau}_{\mathrm{dev,n+1}}\right)$

$\tilde{\mathbf{b}}_{\mathrm{n+1}}^{\mathrm{e}} = \tilde{\mathbf{b}}_{\mathrm{n+1}}^{\mathrm{e,trial}} - \frac{2}{3}\triangle\gamma\mathrm{tr}\left[\tilde{\mathbf{b}}_{\mathrm{n+1}}^{\mathrm{e,trial}}\right]\mathbf{n}_{\mathrm{n+1}}^{\mathrm{trial}}$

$\left(\mathbf{C}_{\mathrm{n+1}}^{\mathrm{p}}\right)^{-1} = \left(\mathbf{C}_{\mathrm{n}}^{\mathrm{p}}\right)^{-1} - \frac{2}{3}\triangle\gamma\mathrm{tr}\left[\tilde{\mathbf{b}}_{\mathrm{n+1}}^{\mathrm{e,trial}}\right]\mathbf{F}_{\mathrm{n+1}}^{-1}\mathbf{n}_{\mathrm{n+1}}^{\mathrm{trial}}\mathbf{F}_{\mathrm{n+1}}^{-\mathrm{T}}$

$\alpha_{n+1} = \alpha_{\mathrm{n}} + \sqrt{\frac{2}{3}}\triangle\gamma$

Calculate the fourth-order consistent elastoplastic tangent moduli $\mathbb{C}$ (see Table 2)

Table 2 The solution algorithm for the fourth-order consistent elastoplastic tangent moduli $\mathbb{C}$

(1) Scaling factors:

$\tilde{\mu} = \frac{1}{3}\mu\mathrm{tr}\left[\tilde{\mathbf{b}}^{\mathrm{e}}\right]$

$\beta_0 = 1 + \frac{k'}{3\tilde{\mu}} \qquad \beta_1 = \left(1 - \frac{1}{\beta_0}\right)\frac{2}{3}\frac{\|\boldsymbol{\tau}_{\mathrm{dev,n+1}}^{\mathrm{trial}}\|}{\tilde{\mu}}\triangle\gamma$

$\beta_2 = \frac{2\tilde{\mu}\triangle\gamma}{\|\boldsymbol{\tau}_{\mathrm{dev,n+1}}^{\mathrm{trial}}\|}$

$\beta_3 = \frac{1}{\beta_0} - \beta_2 + \beta_1 \qquad \beta_4 = \left(\frac{1}{\beta_0} - \beta_3\right)\frac{\|\boldsymbol{\tau}_{\mathrm{dev,n+1}}^{\mathrm{trial}}\|}{\tilde{\mu}}$

(2) Spatial hyperelasticity tensor $\mathbb{C}_{\mathrm{n+1}}^{\mathrm{e,trial}}$:

$\mathbf{II} :=$ fourth-order symmetric identity tensor

$\mathbf{II}_{\mathrm{d}} = \mathbf{II} - \frac{1}{3}\mathbf{I}\otimes\mathbf{I}$

$\mathbb{C}_{\mathrm{vol,n+1}}^{\mathrm{e,trial}} = \kappa\left(J^2\mathbf{I}\otimes\mathbf{I} - \left(J^2-1\right)\mathbf{II}\right)$

$\mathbb{C}_{\mathrm{dev,n+1}}^{\mathrm{e,trial}} = 2\tilde{\mu}\mathbf{II}_{\mathrm{d}} - \frac{2}{3}\left(\boldsymbol{\tau}_{\mathrm{dev,n+1}}^{\mathrm{trial}}\otimes\mathbf{I} + \mathbf{I}\otimes\boldsymbol{\tau}_{\mathrm{dev,n+1}}^{\mathrm{trial}}\right)$

$\mathbb{C}_{\mathrm{n+1}}^{\mathrm{e,trial}} = J^{-1}\left(\mathbb{C}_{\mathrm{vol,n+1}}^{\mathrm{e,trial}} + \mathbb{C}_{\mathrm{dev,n+1}}^{\mathrm{e,trial}}\right)$

(3) Spatial consistent elastoplastic tangent moduli $\mathbb{C}_{\mathrm{n+1}}$:

$\mathbf{n} = \mathbf{n}_{\mathrm{n+1}}^{\mathrm{trial}}$

$\mathbb{C}_{\mathrm{n+1}} = J^{-1}\left(\mathbb{C}_{\mathrm{vol,n+1}}^{\mathrm{e,trial}} + (1-\beta_2)\,\mathbb{C}_{\mathrm{dev,n+1}}^{\mathrm{e,trial}} - 2\tilde{\mu}\beta_3\mathbf{n}\otimes\mathbf{n} - 2\tilde{\mu}\beta_4\left(\mathbf{n}\otimes\mathrm{dev}\left[\mathbf{n}^2\right]\right)^{\mathrm{sym}}\right)$

(4) Material consistent elastoplastic tangent moduli $\mathbb{C}_{\mathrm{n+1}}$:

$\mathbb{C}_{\mathrm{n+1}} = J\mathbf{F}_{\mathrm{n+1}}^{-1}\mathbf{F}_{\mathrm{n+1}}^{-1}\mathbb{C}_{\mathrm{n+1}}\mathbf{F}_{\mathrm{n+1}}^{-1}\mathbf{F}_{\mathrm{n+1}}^{-1}$

necking forms and branches out to the free edges until ultimate failure. Note that the proposed formulation is based on the theory of local plasticity, and therefore the results at the necking zone may be sensitive to the mesh density due to the significant softening in that region. In cases where solution singularity is expected, nonlocal gradient plasticity models are recommended [92] to alleviate this issue.

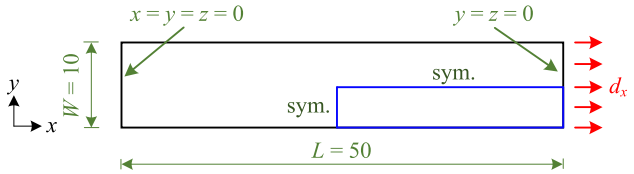

Fig. 2 The geometry and problem setup of the rectangular plate under uniaxial tension. Due to symmetry, only a quarter of the plate is modeled

4.2 Tensile hollow cylinder

The second numerical example considered here is a hollow cylinder model that is fixed at one end and subjected to uniaxial displacement increment at the other end. The same material properties are used as in the first numerical example. Only one octant of the cylinder is modeled leveraging on symmetry and discretized with a total of 500 elements (i.e., 20 elements in the circumferential direction and 25 elements in the length direction). The geometric details and problem setup can be found in Fig. 5.

The effective stress, defined as the applied force divided by the cross-sectional area of the cylinder, is plotted against the displacement norm U_{norm} in Fig. 6, where the obtained results agree very well with the reference solutions [1,2]. The evolution of the internal hardening variable at different loading stages is demonstrated in Fig. 7. Similar to the findings in the rectangular plate example, necking occurs at the central

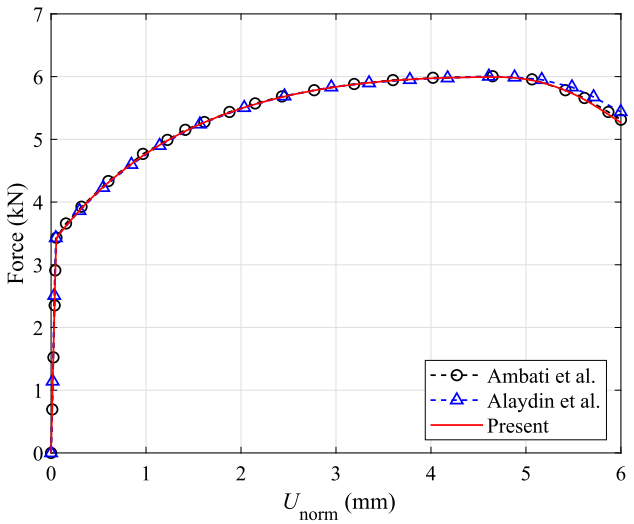

Fig. 3 The load–displacement curve of the tensile plate problem

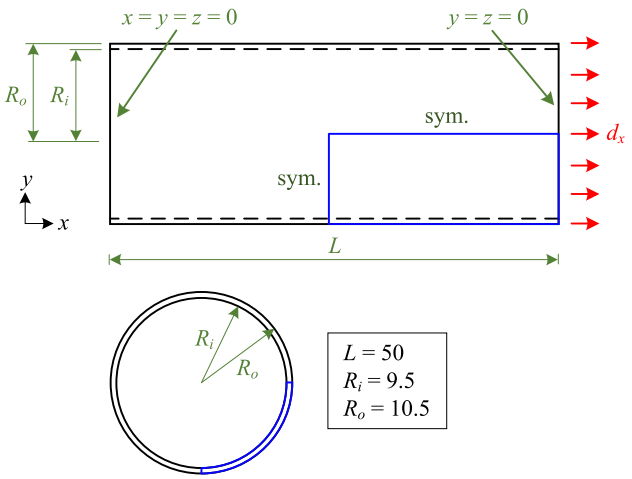

Fig. 5 The geometry and problem setup of the hollow cylinder. Due to symmetry, only one octant of the cylinder is modeled

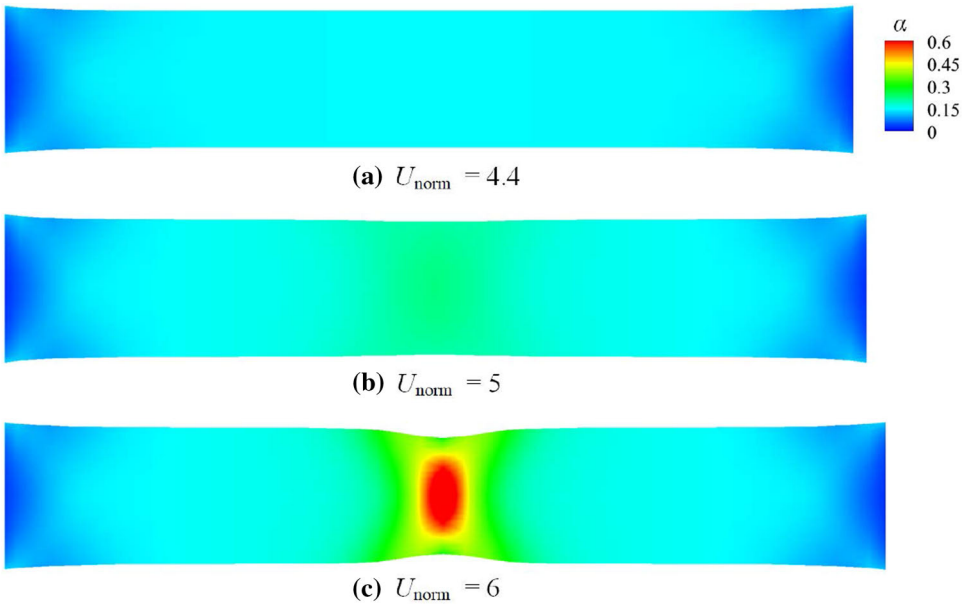

Fig. 4 The contour plots of the hardening variable α at various stages of the loading process in the tensile plate benchmark problem. The hardening variable α is evaluated at the midsurface for visualization

region of the cylinder when the ultimate strength is reached and accounts for the final failure of the model.

4.3 Pinched hemisphere

The pinched hemisphere problem at large elastoplastic deformations is one of the most challenging benchmark examples in both material and geometrically nonlinear shell analysis and has been investigated by a variety of research work [1,9,13,85,93,94], to name a few. The radius and thickness of the hemisphere are $R = 100$ mm and $t = 5$ mm, respectively. The applied material model is: Young's modulus of $E = 100$ N/mm^2, Poisson's ratio of $\nu = 0.2$, and a linear isotropic hardening model of $k(\alpha) = 2 + 30\alpha$. The hemisphere is subjected to two sets of inward and outward opposing point forces of $P = 35$ N at the bottom, respectively. Leveraging on symmetry, only a quarter of the hemisphere is modeled. The detailed geometry and problem setup, as well as the mesh corresponding to a total of 256 NURBS elements used for analysis, can be found in Fig. 8.

The loading/unloading response of the hemisphere is studied. The load–displacement relationship at points A and B in Fig. 8 is plotted in Fig. 9 along with comparisons to the refer-

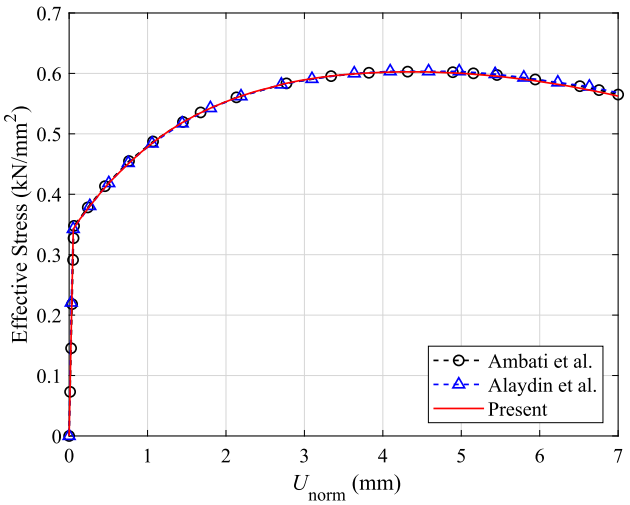

Fig. 6 The load–displacement curve of the hollow cylinder problem

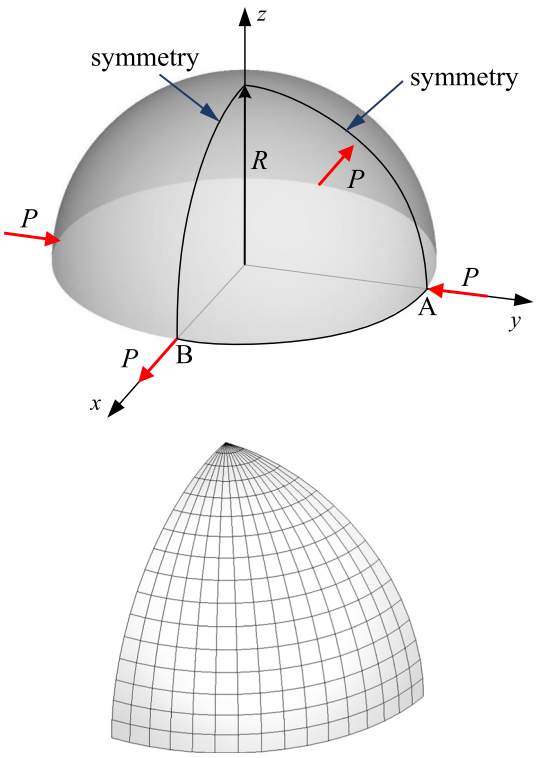

Fig. 8 Pinched hemisphere problem setup and the corresponding mesh used in analysis. The radial displacements at points A and B are recorded

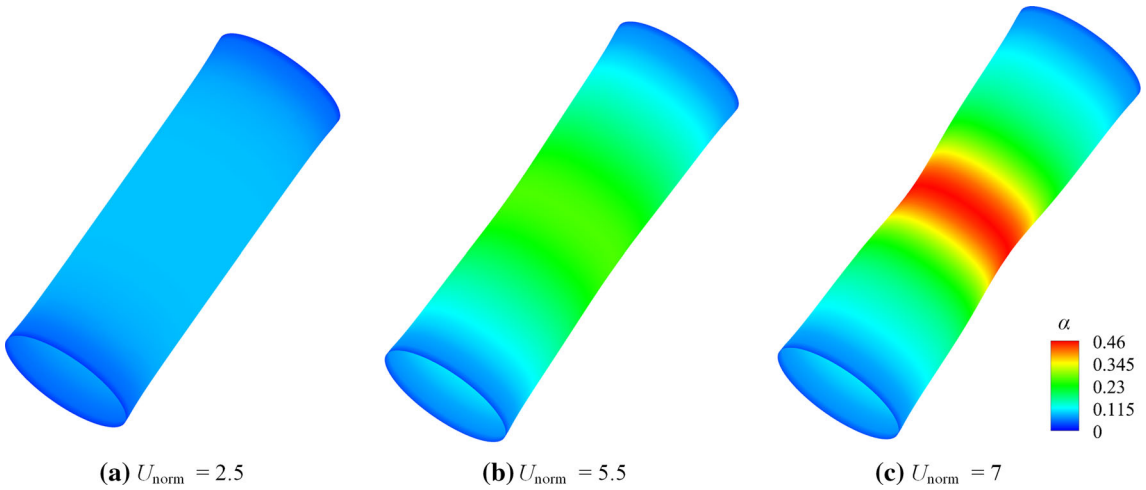

(a) $U_{\text{norm}} = 2.5$ **(b)** $U_{\text{norm}} = 5.5$ **(c)** $U_{\text{norm}} = 7$

Fig. 7 The contour plots of the hardening variable α at various stages of the loading process in the hollow cylinder problem. The hardening variable α is evaluated at the midsurface for visualization

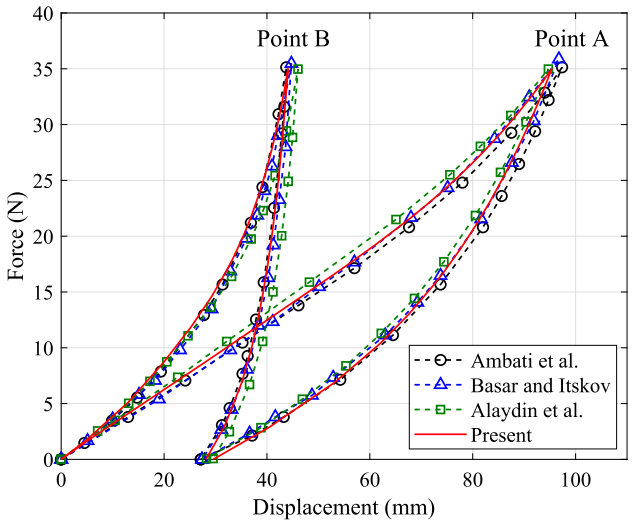

Fig. 9 The load–displacement curves of the pinched hemisphere problem

ence results obtained from Başar and Itskov [93], Ambati et al. [1], and Alaydin et al. [2], where a satisfactory agreement is observed. The evolution of the internal hardening variable α is also illustrated in Fig. 10 at various loading/unloading stages for demonstration purposes. As expected, the plastic strain is localized in the vicinity of the points where external forces are applied and retains itself permanently during unloading.

5 Conclusion

In this work, a large-deformation isogeometric continuum shell formulation that incorporates the theory of finite strain plasticity is developed in a total Lagrangian framework. The key characteristic of the method is the multiplicative decomposition of the deformation gradient into the elastic and plastic parts to properly model plasticity at the finite strain regime. The standard return mapping algorithm and the classical J_2 von Mises plasticity model with nonlinear isotropic hardening are implemented for demonstration. A number of numerical benchmarks are used for testing and the obtained results are compared with published data in literature, which proves the solution accuracy of the present formulation. The

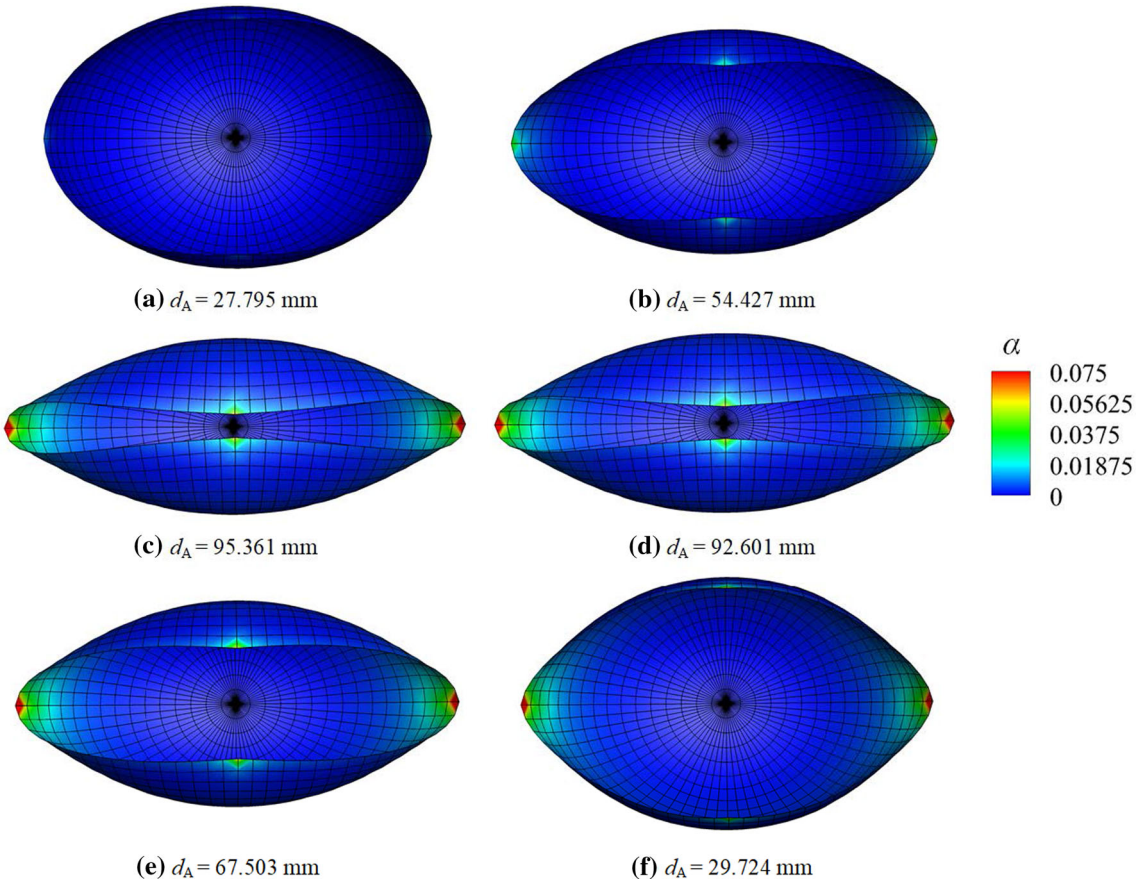

Fig. 10 The contour plots of the hardening variable α at various stages of the loading/unloading process in the pinched hemisphere benchmark. Contours (**a**)–(**c**) are from the loading stage and contours (**d**)–(**f**) are from the unloading stage. The hardening variable α is evaluated at the midsurface for visualization

proposed formulation enables us to obtain high-fidelity 3D strains and stresses in the finite strain plasticity regime while requiring only the surface modeling of thin-walled structures, which greatly reduces the complexity of the geometric modeling process.

The main limitations of the present formulation are that it is rather computationally expensive to solve problems with severe localized plasticity, as compared to computationally efficient KL shell formulations. The reasons are mainly twofold. For one thing, the present isogeometric continuum shell is essentially a solid formulated under curvilinear coordinates, whose solution requires significant computational resource. While not pursued in the current study, reduced quadrature schemes can be used for computational saving. For another, these solid-like formulations are prone to locking issues, especially in the modeling of thin-walled structures. While it is out of the scope of the current study, locking mitigation strategies are recommended to be used together with the present formulation. We plan to address these limitations in future work.

To summarize, although continuum shells are computationally costly compared to KL shells, the ability to accurately compute 3D stresses is clearly a significant advantage in structural failure analysis. It is envisioned that the developed large-deformation elastoplastic continuum shell formulation can be used in a blended shell [24–26] setting where critical structural components with yielding can be modeled using the developed continuum shells for accurate 3D stress prediction and other less critical structural components can be modeled using KL shells for computational efficiency.

Acknowledgements This work is supported by the U.S. Naval Air Systems Command (NAVAIR) under Grant No. N68335-20-C-0899. This support is gratefully acknowledged.

References

1. Ambati M, Kiendl J, De Lorenzis L (2018) Isogeometric Kirchhoff–Love shell formulation for elasto-plasticity. Comput Methods Appl Mech Eng 340:320–339
2. Alaydin MD, Benson DJ, Bazilevs Y (2021) An updated Lagrangian framework for Isogeometric Kirchhoff–Love thin-shell analysis. Comput Methods Appl Mech Eng 384:113977
3. Wagner W, Gruttmann F (2005) A robust non-linear mixed hybrid quadrilateral shell element. Int J Numer Methods Eng 64(5):635–666
4. Kim KD, Lomboy GR (2006) A co-rotational quasi-conforming 4-node resultant shell element for large deformation elasto-plastic analysis. Comput Methods Appl Mech Eng 195(44–47):6502–6522
5. Dal Cortivo N, Felippa CA, Bavestrello H, Silva WTM (2009) Plastic buckling and collapse of thin shell structures, using layered plastic modeling and co-rotational ANDES finite elements. Comput Methods Appl Mech Eng 198(5–8):785–798
6. Brank B, Perić D, Damjanić FB (1997) On large deformations of thin elasto-plastic shells: implementation of a finite rotation model for quadrilateral shell element. Int J Numer Methods Eng 40(4):689–726
7. Klinkel S, Govindjee S (2002) Using finite strain 3D-material models in beam and shell elements. Eng Comput 19(3):254–271
8. Dodds RH Jr (1987) Numerical techniques for plasticity computations in finite element analysis. Comput Struct 26(5):767–779
9. Dujc J, Brank B (2012) Stress resultant plasticity for shells revisited. Comput Methods Appl Mech Eng 247:146–165
10. Zeng Q, Combescure A, Arnaudeau F (2001) An efficient plasticity algorithm for shell elements application to metal forming simulation. Comput Struct 79(16):1525–1540
11. Skallerud B, Myklebust LI, Haugen B (2001) Nonlinear response of shell structures: effects of plasticity modelling and large rotations. Thin-Walled Struct 39(6):463–482
12. Skallerud B, Haugen B (1999) Collapse of thin shell structures-stress resultant plasticity modelling within a co-rotated ANDES finite element formulation. Int J Numer Methods Eng 46(12):1961–1986
13. Simo JC, Kennedy JG (1992) On a stress resultant geometrically exact shell model. Part V. Nonlinear plasticity: formulation and integration algorithms. Comput Methods Appl Mech Eng 96(2):133–171
14. Crisfield MA, Peng X (1992) Efficient nonlinear shell formulations with large rotations and plasticity. In: Owen DRJ et al (eds) Computational plasticity, fundamentals & applications, part 2. Pineridge Press, Swansea, pp 1979–1996
15. Taniguchi Y, Takizawa K, Otoguro Y, Tezduyar TE (2022) A hyperelastic extended Kirchhoff–Love shell model with out-of-plane normal stress: I. Out-of-plane deformation. Comput Mech. https://doi.org/10.1007/s00466-022-02166-x
16. Liu N, Cui X, Xiao J, Lua J, Phan N (2020) A simplified continuum damage mechanics based modeling strategy for cumulative fatigue damage assessment of metallic bolted joints. Int J Fatigue 131:105302
17. Liu N, Xiao J, Cui X, Liu P, Lua J (2019) A continuum damage mechanics (CDM) modeling approach for prediction of fatigue failure of metallic bolted joints. In: AIAA Scitech 2019 Forum, p 0237
18. Liu N, Ren X, Lua J (2020) An isogeometric continuum shell element for modeling the nonlinear response of functionally graded material structures. Compos Struct 237:111893
19. Hosseini S, Remmers JJC, Verhoosel CV, de Borst R (2014) An isogeometric continuum shell element for non-linear analysis. Comput Methods Appl Mech Eng 271:1–22
20. Hosseini S, Remmers JJC, Verhoosel CV, de Borst R (2013) An isogeometric solid-like shell element for nonlinear analysis. Int J Numer Methods Eng 95(3):238–256
21. Bouclier R, Elguedj T, Combescure A (2013) Efficient isogeometric NURBS-based solid-shell elements: mixed formulation and $\bar{B}$-method. Comput Methods Appl Mech Eng 267:86–110
22. Antolin P, Kiendl J, Pingaro M, Reali A (2020) A simple and effective method based on strain projections to alleviate locking in isogeometric solid shells. Comput Mech 65:1621–1631
23. Bouclier R, Elguedj T, Combescure A (2015) An isogeometric locking-free NURBS-based solid-shell element for geometrically nonlinear analysis. Int J Numer Methods Eng 101(10):774–808
24. Liu N, Johnson EL, Rajanna MR, Lua J, Phan N, Hsu M-C (2021) Blended isogeometric Kirchhoff–Love and continuum shells. Comput Methods Appl Mech Eng 385:114005
25. Liu N, Rajanna MR, Johnson EL, Lua J, Phan N, Hsu M-C (2022) Isogeometric blended shells for dynamic analysis: simulating aircraft takeoff and the resulting fatigue damage on the horizontal stabilizer. Comput Mech. https://doi.org/10.1007/s00466-022-02189-4

26. Liu N, Lua J, Rajanna MR, Johnson EL, Hsu M-C, Phan ND (2022) Buffet-induced structural response prediction of aircraft horizontal stabilizers based on immersogeometric analysis and an isogeometric blended shell approach. In: AIAA SCITECH 2022 Forum, p 0852
27. Benson DJ, Hartmann S, Bazilevs Y, Hsu M-C, Hughes TJR (2013) Blended isogeometric shells. Comput Methods Appl Mech Eng 255:133–146
28. Guo Y, Ruess M (2015) Nitsche's method for a coupling of isogeometric thin shells and blended shell structures. Comput Methods Appl Mech Eng 284:881–905
29. Hughes TJR, Cottrell JA, Bazilevs Y (2005) Isogeometric analysis: CAD, finite elements, NURBS, exact geometry and mesh refinement. Comput Methods Appl Mech Eng 194(39–41):4135–4195
30. Liu N, Jeffers AE (2018) A geometrically exact isogeometric Kirchhoff plate: feature-preserving automatic meshing and C^1 rational triangular Bézier spline discretizations. Int J Numer Methods Eng 115(3):395–409
31. Liu N, Jeffers AE (2019) Feature-preserving rational Bézier triangles for isogeometric analysis of higher-order gradient damage models. Comput Methods Appl Mech Eng 357:112585
32. Gómez H, Calo VM, Bazilevs Y, Hughes TJR (2008) Isogeometric analysis of the Cahn–Hilliard phase-field model. Comput Methods Appl Mech Eng 197(49–50):4333–4352
33. Liu J, Dede L, Evans JA, Borden MJ, Hughes TJR (2013) Isogeometric analysis of the advective Cahn–Hilliard equation: spinodal decomposition under shear flow. J Comput Phys 242:321–350
34. Hiemstra RR, Hughes TJR, Reali A, Schillinger D (2021) Removal of spurious outlier frequencies and modes from isogeometric discretizations of second-and fourth-order problems in one, two, and three dimensions. Comput Methods Appl Mech Eng 387:114115
35. Kiendl J, Bletzinger K-U, Linhard J, Wüchner R (2009) Isogeometric shell analysis with Kirchhoff–Love elements. Comput Methods Appl Mech Eng 198:3902–3914
36. Kiendl J, Bazilevs Y, Hsu M-C, Wüchner R, Bletzinger K-U (2010) The bending strip method for isogeometric analysis of Kirchhoff–Love shell structures comprised of multiple patches. Comput Methods Appl Mech Eng 199:2403–2416
37. Kiendl J, Hsu M-C, Wu MCH, Reali A (2015) Isogeometric Kirchhoff–Love shell formulations for general hyperelastic materials. Comput Methods Appl Mech Eng 291:280–303
38. Herrema AJ, Johnson EL, Proserpio D, Wu MCH, Kiendl J, Hsu MC (2019) Penalty coupling of non-matching isogeometric Kirchhoff–Love shell patches with application to composite wind turbine blades. Comput Methods Appl Mech Eng 346:810–840
39. Leonetti L, Liguori FS, Magisano D, Kiendl J, Reali A, Garcea G (2020) A robust penalty coupling of non-matching isogeometric Kirchhoff–Love shell patches in large deformations. Comput Methods Appl Mech Eng 371:113289
40. Casquero H, Wei X, Toshniwal D, Li A, Hughes TJR, Kiendl J, Zhang Y (2020) Seamless integration of design and Kirchhoff–Love shell analysis using analysis-suitable unstructured T-splines. Comput Methods Appl Mech Eng 360:112765
41. Casquero H, Liu L, Zhang Y, Reali A, Kiendl J, Gomez H (2017) Arbitrary-degree T-splines for isogeometric analysis of fully nonlinear Kirchhoff–Love shells. Comput Aided Des 82:140–153
42. Takizawa K, Tezduyar TE, Sasaki T (2019) Isogeometric hyperelastic shell analysis with out-of-plane deformation mapping. Comput Mech 63(4):681–700
43. Benson DJ, Bazilevs Y, De Luycker E, Hsu M-C, Scott M, Hughes TJR, Belytschko T (2010) A generalized finite element formulation for arbitrary basis functions: from isogeometric analysis to XFEM. Int J Numer Methods Eng 83:765–785
44. Benson DJ, Bazilevs Y, Hsu M-C, Hughes TJR (2011) A large deformation, rotation-free, isogeometric shell. Comput Methods Appl Mech Eng 200:1367–1378
45. Morganti S, Auricchio F, Benson DJ, Gambarin FI, Hartmann S, Hughes TJR, Reali A (2015) Patient-specific isogeometric structural analysis of aortic valve closure. Comput Methods Appl Mech Eng 284:508–520
46. Liu N, Jeffers AE (2017) Isogeometric analysis of laminated composite and functionally graded sandwich plates based on a layerwise displacement theory. Compos Struct 176:143–153
47. Liu N, Jeffers AE (2018) Adaptive isogeometric analysis in structural frames using a layer-based discretization to model spread of plasticity. Comput Struct 196:1–11
48. Liu N (2018) Non-uniform rational B-splines and rational Bézier triangles for isogeometric analysis of structural applications. Ph.D. thesis, University of Michigan
49. Kamensky D, Xu F, Lee C-H, Yan J, Bazilevs Y, Hsu M-C (2018) A contact formulation based on a volumetric potential: application to isogeometric simulations of atrioventricular valves. Comput Methods Appl Mech Eng 330:522–546
50. Takizawa K, Tezduyar TE, Uchikawa H, Terahara T, Sasaki T, Yoshida A (2019) Mesh refinement influence and cardiac-cycle flow periodicity in aorta flow analysis with isogeometric discretization. Comput Fluids 179:790–798
51. Liu N, Jeffers AE, Beata PA (2019) A mixed isogeometric analysis and control volume approach for heat transfer analysis of nonuniformly heated plates. Numer Heat Transf Part B Fundam 75(6):347–362
52. Herrema AJ, Kiendl J, Hsu M-C (2019) A framework for isogeometric-analysis-based optimization of wind turbine blade structures. Wind Energy 22:153–170
53. Yan J, Augier B, Korobenko A, Czarnowski J, Ketterman G, Bazilevs Y (2016) FSI modeling of a propulsion system based on compliant hydrofoils in a tandem configuration. Comput Fluids 141:201–211
54. Lorenzo G, Scott MA, Tew K, Hughes TJR, Zhang Y, Liu L, Vilanova G, Gomez H (2016) Tissue-scale, personalized modeling and simulation of prostate cancer growth. Proc Natl Acad Sci 113(48):E7663–E7671
55. Takizawa K, Tezduyar TE, Terahara T (2016) Ram-air parachute structural and fluid mechanics computations with the space-time isogeometric analysis (ST-IGA). Comput Fluids 141:191–200
56. Yan J, Korobenko A, Deng X, Bazilevs Y (2016) Computational free-surface fluid–structure interaction with application to floating offshore wind turbines. Comput Fluids 141:155–174
57. Korobenko A, Yan J, Gohari SMI, Sarkar S, Bazilevs Y (2017) FSI simulation of two back-to-back wind turbines in atmospheric boundary layer flow. Comput Fluids 158:167–175
58. Lai Y, Zhang YJ, Liu L, Wei X, Fang E, Lua J (2017) Integrating CAD with Abaqus: a practical isogeometric analysis software platform for industrial applications. Comput Math Appl 74:1648–1660
59. Guo Y, Heller J, Hughes TJR, Ruess M, Schillinger D (2018) Variationally consistent isogeometric analysis of trimmed thin shells at finite deformations, based on the STEP exchange format. Comput Methods Appl Mech Eng 336:39–79
60. Teschemacher T, Bauer AM, Oberbichler T, Breitenberger M, Rossi R, Wüchner R, Bletzinger K-U (2018) Realization of CAD-integrated shell simulation based on isogeometric B-Rep analysis. Adv Model Simul Eng Sci 5:19
61. Xu F, Morganti S, Zakerzadeh R, Kamensky D, Auricchio F, Reali A, Hughes TJR, Sacks MS, Hsu M-C (2018) A framework for designing patient-specific bioprosthetic heart valves using immersogeometric fluid–structure interaction analysis. Int J Numer Methods Biomed Eng 34:e2938
62. Otoguro Y, Takizawa K, Tezduyar TE, Nagaoka K, Mei S (2019) Turbocharger turbine and exhaust manifold flow computation with the space-time variational multiscale method and isogeometric analysis. Comput Fluids 179:764–776

63. Kanai T, Takizawa K, Tezduyar TE, Tanaka T, Hartmann A (2019) Compressible-flow geometric-porosity modeling and spacecraft parachute computation with isogeometric discretization. Comput Mech 63:301–321
64. Yu Y, Zhang YJ, Takizawa K, Tezduyar TE, Sasaki T (2020) Anatomically realistic lumen motion representation in patient-specific space-time isogeometric flow analysis of coronary arteries with time-dependent medical-image data. Comput Mech 65:395–404
65. Otoguro Y, Takizawa K, Tezduyar TE, Nagaoka K, Avsar R, Zhang Y (2019) Space-time VMS flow analysis of a turbocharger turbine with isogeometric discretization: computations with time-dependent and steady-inflow representations of the intake/exhaust cycle. Comput Mech 64:1403–1419
66. Yan J, Lin S, Bazilevs Y, Wagner GJ (2019) Isogeometric analysis of multi-phase flows with surface tension and with application to dynamics of rising bubbles. Comput Fluids 179:777–789
67. Lorenzo G, Hughes TJR, Dominguez-Frojan P, Reali A, Gomez H (2019) Computer simulations suggest that prostate enlargement due to benign prostatic hyperplasia mechanically impedes prostate cancer growth. Proc Natl Acad Sci 116:1152–1161
68. Terahara T, Takizawa K, Tezduyar TE, Tsushima A, Shiozaki K (2020) Ventricle-valve-aorta flow analysis with the space-time isogeometric discretization and topology change. Comput Mech 65:1343–1363
69. Terahara T, Takizawa K, Tezduyar TE, Bazilevs Y, Hsu M-C (2020) Heart valve isogeometric sequentially-coupled FSI analysis with the space-time topology change method. Comput Mech 65:1167–1187
70. Pigazzini MS, Kamensky D, van Iersel DAP, Alaydin MD, Remmers JJC, Bazilevs Y (2019) Gradient-enhanced damage modeling in Kirchhoff–Love shells: application to isogeometric analysis of composite laminates. Comput Methods Appl Mech Eng 346:152–179
71. Leidinger LF, Breitenberger M, Bauer AM, Hartmann S, Wüchner R, Bletzinger K-U, Duddeck F, Song L (2019) Explicit dynamic isogeometric B-Rep analysis of penalty-coupled trimmed NURBS shells. Comput Methods Appl Mech Eng 351:891–927
72. Wu MCH, Muchowski HM, Johnson EL, Rajanna MR, Hsu M-C (2019) Immersogeometric fluid–structure interaction modeling and simulation of transcatheter aortic valve replacement. Comput Methods Appl Mech Eng 357:112556
73. Balu A, Nallagonda S, Xu F, Krishnamurthy A, Hsu M-C, Sarkar S (2019) A deep learning framework for design and analysis of surgical bioprosthetic heart valves. Sci Rep 9:18560
74. Johnson EL, Wu MCH, Xu F, Wiese NM, Rajanna MR, Herrema AJ, Ganapathysubramanian B, Hughes TJR, Sacks MS, Hsu M-C (2020) Thinner biological tissues induce leaflet flutter in aortic heart valve replacements. Proc Natl Acad Sci 117:19007–19016
75. Nitti A, Kiendl J, Reali A, de Tullio MD (2020) An immersed-boundary/isogeometric method for fluid–structure interaction involving thin shells. Comput Methods Appl Mech Eng 364:112977
76. Proserpio D, Ambati M, De Lorenzis L, Kiendl J (2020) A framework for efficient isogeometric computations of phase-field brittle fracture in multipatch shell structures. Comput Methods Appl Mech Eng 372:113363
77. Johnson EL, Hsu M-C (2020) Isogeometric analysis of ice accretion on wind turbine blades. Comput Mech 66:311–322
78. Zhang W, Motiwale S, Hsu M-C, Sacks MS (2021) Simulating the time evolving geometry, mechanical properties, and fibrous structure of bioprosthetic heart valve leaflets under cyclic loading. J Mech Behav Biomed Mater 123:104745
79. Behzadinasab M, Hillman M, Bazilevs Y (2021) IGA-PD penalty-based coupling for immersed air-blast fluid-structure interaction: a simple and effective solution for fracture and fragmentation. J Mech 37:680–692
80. Johnson EL, Laurence DW, Xu F, Crisp CE, Mir A, Burkhart HM, Lee C-H, Hsu M-C (2021) Parameterization, geometric modeling, and isogeometric analysis of tricuspid valves. Comput Methods Appl Mech Eng 384:113960
81. Otoguro Y, Mochizuki H, Takizawa K, Tezduyar TE (2020) Space-time variational multiscale isogeometric analysis of a tsunami-shelter vertical-axis wind turbine. Comput Mech 66:1443–1460
82. Bazilevs Y, Takizawa K, Wu MCH, Kuraishi T, Avsar R, Xu Z, Tezduyar TE (2021) Gas turbine computational flow and structure analysis with isogeometric discretization and a complex-geometry mesh generation method. Comput Mech 67:57–84
83. Johnson EL, Rajanna MR, Yang C-H, Hsu M-C (2022) Effects of membrane and flexural stiffnesses on aortic valve dynamics: identifying the mechanics of leaflet flutter in thinner biological tissues. Forces Mech 6:100053
84. Huynh GD, Zhuang X, Bui HG, Meschke G, Nguyen-Xuan H (2020) Elasto-plastic large deformation analysis of multi-patch thin shells by isogeometric approach. Finite Elem Anal Des 173:103389
85. Caseiro JF, Valente RAF, Reali A, Kiendl J, Auricchio F, Alves de Sousa RJ (2015) Assumed natural strain nurbs-based solid-shell element for the analysis of large deformation elasto-plastic thin-shell structures. Comput Methods Appl Mech Eng 284:861–880
86. Simo JC, Hughes TJR (1998) Computational inelasticity. Springer, New York
87. Liu N, Plucinsky P, Jeffers AE (2017) Combining load-controlled and displacement-controlled algorithms to model thermal-mechanical snap-through instabilities in structures. J Eng Mech 143(8):04017051
88. Simo JC (1988) A framework for finite strain elastoplasticity based on maximum plastic dissipation and the multiplicative decomposition: part I. Continuum formulation. Comput Methods Appl Mech Eng 66(2):199–219
89. Simo JC (1988) A framework for finite strain elastoplasticity based on maximum plastic dissipation and the multiplicative decomposition: Part II: computational aspects. Comput Methods Appl Mech Eng 68(1):1–31
90. Holzapfel GA (2000) Nonlinear solid mechanics: a continuum approach for engineering. Wiley, Chichester
91. Behzadinasab M, Alaydin M, Trask N, Bazilevs Y (2022) A general-purpose, inelastic, rotation-free Kirchhoff–Love shell formulation for peridynamics. Comput Methods Appl Mech Eng 389:114422
92. Bažant ZP, Jirásek M (2002) Nonlocal integral formulations of plasticity and damage: survey of progress. J Eng Mech 128(11):1119–1149
93. Başar Y, Itskov M (1999) Constitutive model and finite element formulation for large strain elasto-plastic analysis of shells. Comput Mech 23(5):466–481
94. Klinkel S, Gruttmann F, Wagner W (2006) A robust non-linear solid shell element based on a mixed variational formulation. Comput Methods Appl Mech Eng 195(1–3):179–201